

# Widespread decline of Congo rainforest greenness in the past decade

Liming Zhou<sup>1</sup>, Yuhong Tian<sup>2</sup>, Ranga B. Myneni<sup>3</sup>, Philippe Ciais<sup>4</sup>, Sassan Saatchi<sup>5</sup>, Yi Y. Liu<sup>6</sup>, Shilong Piao<sup>7</sup>, Haishan Chen<sup>8</sup>, Eric F. Vermote<sup>9</sup>, Conghe Song<sup>10,11</sup> & Taehee Hwang<sup>12</sup>

**Tropical forests are global epicentres of biodiversity and important modulators of climate change<sup>1</sup>, and are mainly constrained by rainfall patterns<sup>1–3</sup>. The severe short-term droughts that occurred recently in Amazonia have drawn attention to the vulnerability of tropical forests to climatic disturbances<sup>4–9</sup>. The central African rainforests, the second-largest on Earth, have experienced a long-term drying trend<sup>10,11</sup> whose impacts on vegetation dynamics remain mostly unknown because *in situ* observations are very limited. The Congolese forest, with its drier conditions and higher percentage of semi-evergreen trees<sup>12,13</sup>, may be more tolerant to short-term rainfall reduction than are wetter tropical forests<sup>11</sup>, but for a long-term drought there may be critical thresholds of water availability below which higher-biomass, closed-canopy forests transition to more open, lower-biomass forests<sup>1,2,14</sup>. Here we present observational evidence for a widespread decline in forest greenness over the past decade based on analyses of satellite data (optical, thermal, microwave and gravity) from several independent sensors over the Congo basin. This decline in vegetation greenness, particularly in the northern Congolese forest, is generally consistent with decreases in rainfall, terrestrial water storage, water content in aboveground woody and leaf biomass, and the canopy backscatter anomaly caused by changes in structure and moisture in upper forest layers. It is also consistent with increases in photosynthetically active radiation and land surface temperature. These multiple lines of evidence indicate that this large-scale vegetation browning, or loss of photosynthetic capacity, may be partially attributable to the long-term drying trend. Our results suggest that a continued gradual decline of photosynthetic capacity and moisture content driven by the persistent drying trend could alter the composition and structure of the Congolese forest to favour the spread of drought-tolerant species<sup>1,2,14</sup>.**

The impact of changes in precipitation patterns, such as short-term and long-term droughts, on tropical rainforests is poorly understood and currently under debate<sup>4–11</sup>. Systematic monitoring of the forests is essential to understanding their response to climate change, and remote sensing remains the only viable way of synoptically and repeatedly monitoring vast remote regions such as the Congo basin<sup>10,11</sup>. This study uses Enhanced Vegetation Index (EVI)<sup>15</sup> data derived from a satellite-borne sensor, MODerate resolution Imaging Spectroradiometer (MODIS), for the period 2000–2012. EVI correlates well with leaf area index, canopy photosynthetic activity and primary productivity<sup>16–18</sup>. We focus our study on intact forested regions in the Congo basin (5° N–6° S, 14° E–31° E) during April–May–June, which represents the first of two rain and peak growing seasons and exhibits the highest percentage of forested area with high-quality EVI data (Extended Data Fig. 1). EVI lags the bimodal seasonal cycle of rainfall by about one month and has a smoother

seasonal variation than rainfall, consistent with observed phenological (leaf area index) responses of tropical trees to increasing soil moisture<sup>19</sup>.

We also use three gauge-measured and satellite-derived rainfall data sets<sup>20–22</sup> and other satellite products: terrestrial water storage (TWS)<sup>23,24</sup>, aerosol optical thickness (AOT), cloud optical thickness (COT), photosynthetically active radiation (PAR) and land surface temperature (LST) as climate drivers; and vegetation optical depth (VOD)<sup>25</sup> and canopy backscatter anomaly (CBA)<sup>11</sup> (together with EVI) as vegetation variables (see Methods). VOD represents water content in aboveground woody and leaf biomass and is sensitive to long-term climate changes<sup>25</sup>. CBA reflects the changes in structure and moisture in upper forest layers and thus can help identify large-scale tree mortality<sup>8,11</sup>. TWS quantifies large-scale and low-frequency total ground, surface and vegetation water storage anomalies<sup>23,24</sup>. Unlike EVI, the microwave products CBA and VOD are least affected by atmospheric and weather conditions<sup>11,25</sup>. Most of the data are independent and thus allow a multi-factor analysis.

Although differing in data source, duration, spatial resolution and processing, the three rainfall data sets show strong and similar interannual variations during April–May–June over the study region, with the strongest negative anomalies falling in the last decade of the long-term 1950 to 2012 mean (Fig. 1a). The regional-mean rainfall declined significantly by  $-0.32 \pm 0.10$  mm per day per decade ( $7.2 \pm 2.2\%$ ,  $P = 0.002$ ) or by  $-0.56$  mm per day (12.6%) between the last and first decades for the period 1985–2012. The drying trend (Fig. 1b and c) is widespread across the study region, with 25%–62% of forested area showing a significant negative trend ( $P < 0.05$ ).

The spatial patterns of EVI trends are shown in Fig. 2, together with the corresponding trends in rainfall, TWS and CBA for the period 2000–2012. Because most of the satellite data sets are only 10–13 years long, linear regressions are used to quantify simply whether there is a trend within each data record; such a trend, however, cannot be extrapolated linearly over longer periods. Although the time series is short, EVI declined over 92% of the study area from 2000 to 2012 and in 97% of the area from 2003 to 2012, with 39% and 54% of the area showing a significant negative trend ( $P < 0.1$ ), respectively, indicating that the EVI decrease became broader in space and stronger over time. The two rainfall data show similar large-scale declines from 2000 to 2012. TWS declined over most of the study area, particularly over the northern Congo. CBA also declined over 85% of the area from 2001 to 2009. Overall about 12%–28% of the forested area exhibited a significant negative trend ( $P < 0.1$ ) for rainfall, TWS and CBA.

Figure 3 shows interannual variations of climate and vegetation variables at regional level for the period 2000–2012. EVI declined significantly by  $-0.021 \pm 0.007$  per decade ( $P = 0.016$ ; 2000–2012) and  $-0.038 \pm 0.009$  ( $P = 0.002$ ; 2003–2012). Rainfall, TWS, CBA and VOD also

<sup>1</sup>Department of Atmospheric and Environmental Sciences, University at Albany, State University of New York (SUNY), Albany, New York 12222, USA. <sup>2</sup>I. M. Systems Group (IMSG), National Oceanic and Atmospheric Administration/National Environmental Satellite, Data, and Information Service/The Center for Satellite Applications and Research (NOAA/NESDIS/STAR), 5830 University Research Court, College Park, Maryland 20740, USA. <sup>3</sup>Department of Earth and Environment, Boston University, Boston, Massachusetts 02215, USA. <sup>4</sup>Laboratoire des Sciences du Climat et de l'Environnement (LSE), CEA-CNRS-UVSQ, 91191 Gif sur Yvette Cedex, France. <sup>5</sup>Jet Propulsion Laboratory, Pasadena, California 91109, USA. <sup>6</sup>ARC Centre of Excellence for Climate Systems Science & Climate Change Research Centre, University of New South Wales, Sydney, New South Wales 2052, Australia. <sup>7</sup>Department of Ecology, College of Urban and Environmental Sciences, Peking University, Beijing 100871, China. <sup>8</sup>Key Laboratory of Meteorological Disaster, Ministry of Education, Nanjing University of Information Science and Technology, Nanjing 210044, China. <sup>9</sup>NASA Goddard Space Flight Center, Code 619, Greenbelt, Maryland 20771, USA. <sup>10</sup>Department of Geography, University of North Carolina at Chapel Hill, Chapel Hill, North Carolina 29599, USA. <sup>11</sup>School of Forestry and Landscape Architecture, Anhui Agricultural University, Hefei, Anhui 230036, China. <sup>12</sup>Institute for the Environment, University of North Carolina at Chapel Hill, Chapel Hill, North Carolina 29599, USA.

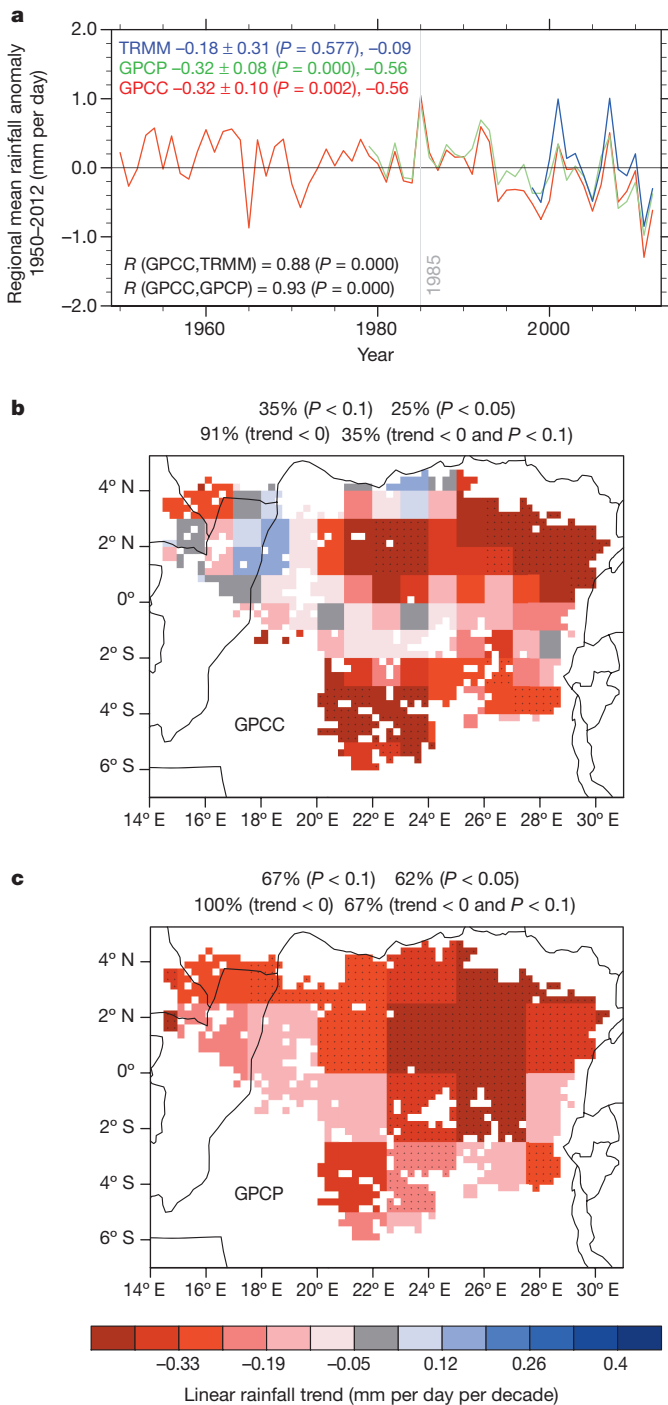


**Figure 1 | April–May–June rainfall anomalies and linear trends per decade.** **a**, Regional mean anomalies from three data sets (GPCC, 1950–2012; GPCP, 1979–2012; and TRMM, 1998–2012). The linear trend ( $\pm$ one standard deviation) and its significance level  $P$  for the period 1985–2012, the decadal difference (2003–2012 minus 1985–1994 averages) for GPCC and GPCP, and the 3-year difference (2009–2012 minus 1998–2001 averages) for TRMM are shown. The correlation coefficient  $R$  between GPCC and TRMM and between GPCC and GPCP are also shown. **b**, **c**, Spatial patterns of linear trends in GPCC (**b**) and GPCP (**c**) for the period 1985–2012 when the rainfall data showed a gradually decreasing trend. In **b** and **c**, pixels with plus symbol have a linear trend that is statistically significant at  $P < 0.05$ . The percentages of pixels with trends at  $P < 0.05$  and  $P < 0.1$  over the study region are listed, as are the percentages of pixels with negative trends.

decreased but most trends are insignificant because of strong inter-annual variability and short data records. However, the rainfall tended towards more negative anomalies over time and reached its lowest levels

in the last few years. EVI demonstrates similar changes and so does TWS. Similar decreases are also seen for these variables in differences between the last and first three years. Most year-to-year correlations between EVI and other variables in April–May–June (no lag) are statistically significant: EVI–rainfall ( $R = 0.46$ – $0.48$ ,  $P = 0.097$ – $0.114$ ), EVI–TWS ( $R = 0.68$ – $0.88$ ,  $P = 0.001$ – $0.032$ ) and EVI–CBA ( $R = 0.66$ ,  $P = 0.037$ ). VOD correlates weakly with EVI ( $R = 0.34$ ,  $P = 0.312$ ) from 2000 to 2010, but its longer time series shows minima in the last few years (Fig. 4a). The low-frequency nature of TWS changes corresponds well to that of EVI variations and thus EVI correlates well with TWS also at the pixel scale (Extended Data Fig. 2).

The amount of radiation for plant growth and transpiration is determined by atmospheric conditions (clouds and aerosols) and latitude. COT showed a significant and widespread decreasing trend for the period 2000–2012, whereas AOT changed little, except in 2004 because of two volcanic eruptions (Extended Data Fig. 3). Consequently, PAR increased by  $+7.0 \pm 3.0\%$  ( $P = 0.049$ ) from 2003 to 2012 and this increase is stronger over the southern Congo than the northern Congo (Extended Data Fig. 4). Increasing PAR can enhance radiation-limited canopy photosynthesis<sup>17,18</sup> and evapotranspiration as long as the system remains energy-limited. Beyond the point where soil moisture becomes limiting, it will no longer increase transpiration and may actually enhance water stress for plant growth over the southern Congo where rainfall reduction is weaker than in the northern Congo. Consequently, LST increased over the majority of pixels during 2003–2012, particularly in the northern Congo, where strong drying trends are observed (Extended Data Fig. 4).

We also analysed the newly developed VOD data<sup>25</sup> for the period 1988–2010 in view of the short EVI record. The regional mean April–May–June VOD decreased steadily from 1988 to 2002, recovered slightly between 2003 and 2006, and reached the lowest levels thereafter (Fig. 4a), mirroring the low-frequency signal of rainfall variations. It decreased significantly,  $-0.003 \pm 0.001$  ( $-0.3 \pm 0.1\%$ ) per decade ( $P = 0.002$ ) or by  $-0.003$  ( $-0.3\%$ ) between the last and first decades. The magnitude of VOD trend is small owing to its large spatial variability, and in particular, VOD represents mostly above-ground woody biomass water content<sup>26</sup>. At the pixel level, VOD decreased significantly ( $P < 0.1$ ) over 38% of the study area with a larger magnitude (Fig. 4b). The annual mean VOD shows similar trends and variability (Extended Data Fig. 5). We note that VOD may be underestimated over open water areas<sup>25</sup>. However, the decline in rainfall would result in less standing open water spatially and temporally and thus larger increases in VOD values rather than the observed decreasing trend (Supplementary Information section A).

The lack of a strong spatial coupling between rainfall and EVI/VOD changes (Figs 1b and c, 2a–d and 4b) is not surprising given the large spatiotemporal variability of rainfall<sup>10</sup>, the complex lagged relationships between rainfall and vegetation phenology and photosynthetic activity<sup>1–3</sup>, and the different responses of various plant species to drought<sup>27</sup>. Deep roots in some forests allow trees to access ground water and delay the inception of moisture stress. Although EVI and VOD provide complementary information on vegetation dynamics, EVI is more responsive to changes in canopy cover/greenness and short-term precipitation variations whereas VOD is more sensitive to changes in woody vegetation and long-term precipitation variation<sup>26</sup>. Consequently there are lagged correlations between EVI/VOD in April–May–June and mean rainfall in earlier months: April–May–June EVI correlated significantly ( $R = 0.69$ ,  $P = 0.009$ ) with March–April–May rainfall and April–May–June VOD correlated significantly ( $R = 0.49$ ,  $P = 0.017$ ) with rainfall during December–January–February–March–April–May (Figs 3b and 4a). The TWS–rainfall correlations are similarly weak, because TWS in wet tropical regions represents surface and groundwater changes rather than small-scale and short-term rainfall anomalies<sup>23,24</sup>. In particular, the moisture available in the root zone for plant photosynthesis is determined not only by the sum of rainfall but also by runoff and evapotranspiration<sup>24</sup>. Over the Congo, TWS decreased most in low elevation valleys, not over the areas where rainfall decreased most (Fig. 2c–e), because local upland

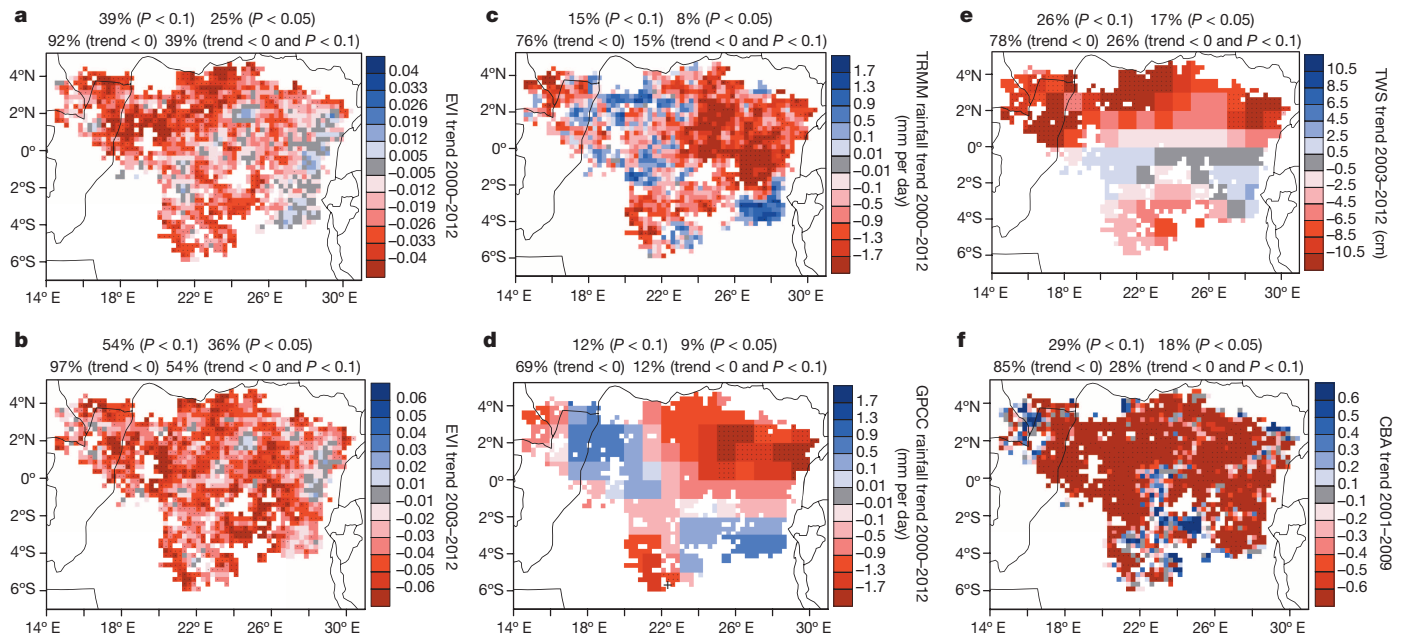


**Figure 2 | Spatial patterns of linear trends per decade in April–May–June for the period 2000–2012.** Pixels with plus symbols have a linear trend that is statistically significant ( $P < 0.1$ ). The percentages of pixels with trends at  $P < 0.05$  and  $P < 0.1$  and the percentages of pixels with negative trends over the study region are shown. **a, b**, EVI. **c, d**, TRMM and GPCC rainfall. **e**, Ensemble

mean TWS from three data processing centres. **f**, CBA. (EVI and CBA are unitless.) The CBA for 2000 was not used because the data during the period 2001–2009 in general show a decreasing trend (Fig. 3d). TWS from the three data processing centres shows similar large-scale patterns of linear trends (Extended Data Fig. 2).

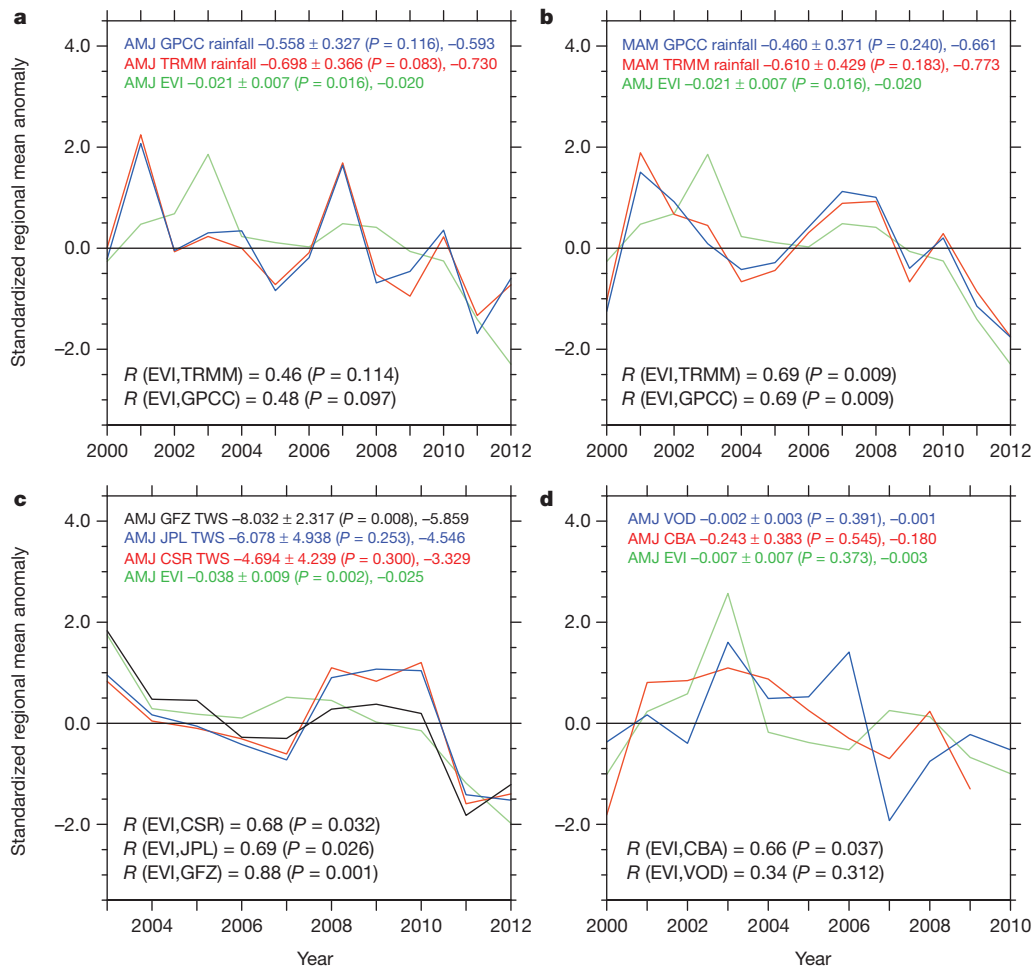


**Figure 3 | Regional mean anomalies in EVI, rainfall, TWS, CBA and VOD.** (VOD is unitless; rainfall has units of millimetres per day, TWS has units of centimetres.) The linear trend ( $\pm$ one standard deviation) per decade and its significance level  $P$  are shown, followed by the mean value difference between the last and first three years. The correlation coefficient  $R$  and its  $P$  value between EVI and other variables are shown. All variables are standardized for visualization purposes, owing to the differences in magnitude. **a**, April–May–June (AMJ) EVI and April–May–June rainfall. **b**, April–May–June EVI and March–April–May (MAM) rainfall. **c**, April–May–June EVI and April–May–June TWS from three data processing centres: the University of Texas’ Center for Space Research (CSR), NASA’s Jet Propulsion Laboratory (JPL) and Germany’s GeoForschungsZentrum (GFZ). **d**, EVI, VOD and CBA in April–May–June.

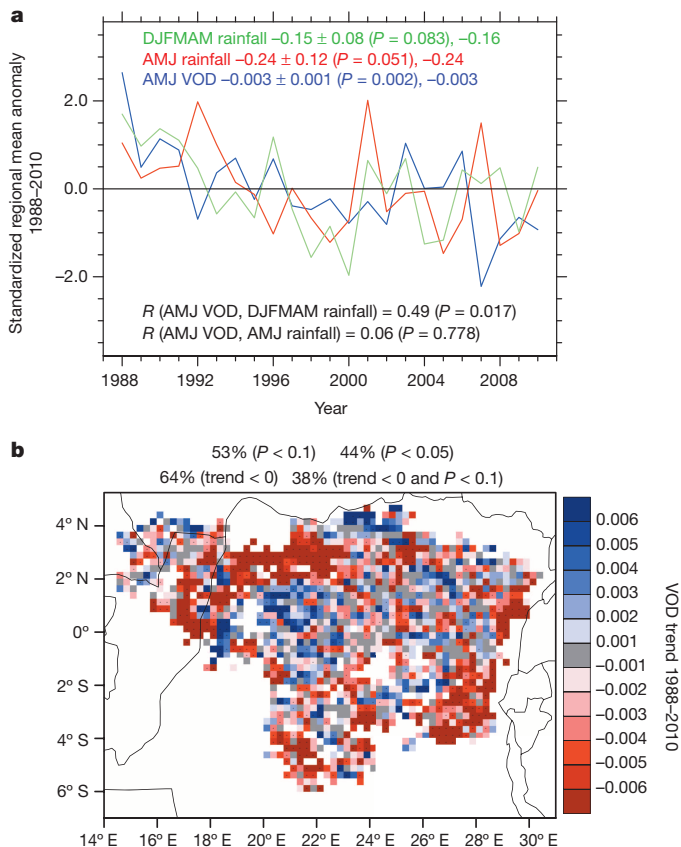


**Figure 4 | VOD anomalies and linear trends per decade in April–May–June for the period 1988–2010.** **a**, Regional mean VOD anomaly in April–May–June and its relationship with rainfall from GPCP in April–May–June (no lag) and DJFMAM (December–January–February–March–April–May, with lags). The linear trend ( $\pm$  one standard deviation), its significance level  $P$  and the decadal difference (2001–2010 minus 1988–1997 averages) are shown. The correlation coefficient  $R$  and its  $P$  value is also shown. **b**, Spatial patterns of linear trend per decade of VOD for the period 1988–2010. Pixels with plus symbols have a linear trend that is statistically significant at  $P < 0.05$ ; the percentages of pixels with trends at  $P < 0.05$  and  $P < 0.1$  and the percentages of pixels with negative trends over the study region are shown.

runoff is the main source of the Congo wetland water<sup>28</sup>. Furthermore, the effects of long-term drought on vegetation are more complex than short-term drought<sup>11</sup> and different satellite products measure different properties of vegetation and moisture<sup>11,25</sup> at different spatiotemporal resolutions, which make it difficult to infer a strong coupling between vegetation and moisture parameters at pixel level. Nevertheless, the combined areas with a decreasing trend in rainfall and TWS indicate a widespread and increasing water deficit, which agrees consistently with the large-scale EVI decreases.

Most of the EVI decline reflects real changes in vegetation characteristics rather than data errors<sup>7</sup>, residual atmospheric artefacts due to aerosol and cloud contaminations<sup>6</sup>, sun-view angle effects, sensor degradation, deforestation, and natural fires (Extended Data Figs 6–9 and Supplementary Information sections B–E). The persistent browning of the Congolese forests might reflect a slow adjustment to the long-term drying trend, rather than a response to episodic events such as the Amazon droughts. It is generally consistent with the gradual temporal changes in moisture, vegetation and radiation parameters observed from several independent satellite products. In particular, VOD and CBA, together with high-resolution satellite images from Landsat (Extended Data Fig. 10 and Supplementary Information section D), only show small and gradual changes in canopy structure instead of large-scale tree mortality as in the Amazon<sup>8</sup>. The large decline in EVI and VOD in recent years is also paralleled by an acceleration of climate drivers such as PAR, rainfall

and TWS changes. Furthermore, the persistent decrease in COT and strong increase in PAR support the observed decrease in rainfall, warming of the forested landscape and the increase in evapotranspiration demand over the Congo.

Water deficit stress will be manifested in trees as less turgid leaves, and if the stress is beyond some threshold, the trees may drop their leaves. This behaviour can be detected as a decline in EVI. A slow decline of EVI over time implies loss of photosynthetic capacity. Such a temporary loss due to short-term drought may have minimal effects on vegetation because the trees may leaf out as soon as rainfall recovers. However, under the stress of an increased severity of water deficit, the gradual loss of photosynthetic capacity and water content over a long period may alter forest species composition and structure<sup>1,2,14</sup> and thus affect biodiversity and carbon storage<sup>1,29</sup>. Drier conditions may favour deciduous trees at the expense of evergreen trees<sup>2,14</sup>. For example, over a 20-year period of exposure to a drying trend, the Ghanaian forest species shifted from wetter-forest-affiliated vegetation to deciduous and drier-forest canopy species<sup>14</sup>. Detection and attribution of such impacts require long-term ground observations and drought manipulative experiments (as for the Amazon forests<sup>30</sup>); these, however, are not available for Congolese forests, and should be a research priority.

## METHODS SUMMARY

We analyse gridded data from ground observations and different satellite sensors over the Congo (see Methods for details): (1) MODIS products of EVI<sup>15</sup> (monthly, 2000–2012), LST (monthly, 2003–2012), and land cover (yearly, 2001–2012) at 0.05° resolution, and AOT and COT at 1° resolution (monthly, 2000–2012); (2) monthly rainfall from GPCP<sup>20</sup> (1°, 1950–2012), GPCP<sup>21</sup> (2.5°, 1979–2012) and TRMM<sup>22</sup> (0.25°, 1998–2012); (3) monthly TWS<sup>23</sup> and PAR (1°, 2003–2012); and (4) monthly data of VOD<sup>25</sup> (0.25°, 1988–2010) and CBA<sup>11</sup> (0.04°, 2000–2009). We focused only on the intact Congolese forest pixels (5° N–6° S, 14° E–31° E) during April–May–June using a high-quality EVI mask based on EVI quality assurance information. For each year, monthly high-quality 0.05° EVI anomalies were aggregated into one single seasonal (April–May–June) image at 0.25° resolution. The other variables were similarly averaged into seasonal anomalies and then re-projected into the study region at 0.25° resolution. Regional and spatial aggregations were applied only to the masked high-quality EVI pixels. Two methods were used to quantify the temporal changes at both the pixel level and the regional level: first, a mean value difference between two individual periods; and second, a linear trend estimated using ordinary least squares over a certain time period. For the first method, the two periods are defined as the last and first three years if the data record is less than 20 years long, and the last and first decades otherwise. For the second method, the Student's  $t$ -statistic was calculated to quantify the probability  $P$  of whether the trend is statistically significantly different from zero or simply due to random noise. Both methods should provide consistent results if there is a persistent trend in the data. A linear correlation and its significance level ( $P$  value) were calculated between two time series to quantify their association. The acronyms and abbreviations are listed in Supplementary Information Supplementary Table 4.

**Online Content** Any additional Methods, Extended Data display items and Source Data are available in the online version of the paper; references unique to these sections appear only in the online paper.

Received 8 August 2013; accepted 21 March 2014.

Published online 23 April 2014.

- Lewis, S. L. Tropical forests and the changing earth system. *Phil. Trans. R. Soc. Lond. B* **361**, 195–210 (2006).
- Enquist, B. J. & Enquist, C. A. F. Long-term change within a neotropical forest: assessing differential functional and floristic responses to disturbance and drought. *Glob. Change Biol.* **17**, 1408–1424 (2011).
- Lewis, S. L. *et al.* Above-ground biomass and structure of 260 African tropical forests. *Phil. Trans. R. Soc. Lond. B* **368**, 20120295 (2013).
- Brando, P. M. *et al.* Seasonal and interannual variability of climate and vegetation indices across the Amazon. *Proc. Natl Acad. Sci. USA* **107**, 14685–14690 (2010).
- Xu, L. *et al.* Widespread decline in greenness of Amazonian vegetation due to the 2010 drought. *Geophys. Res. Lett.* **38**, L07402 (2011).
- Samanta, A., Ganguly, S., Vermote, E., Nemani, R. R. & Myneni, R. B. Why is remote sensing of Amazon forest greenness so challenging? *Earth Interact.* **16**, 1–14 (2012).
- Atkinson, P. M., Dash, J. & Jeganathan, C. Amazon vegetation greenness as measured by satellite sensors over the last decade. *Geophys. Res. Lett.* **38**, L19105 (2011).

8. Saatchi, S. *et al.* Persistent effects of a severe drought on Amazonian forest canopy. *Proc. Natl Acad. Sci. USA* **110**, 565–570 (2013).
9. Morton, D. C. *et al.* Amazon forests maintain consistent canopy structure and greenness during the dry season. *Nature* **506**, 221–224 (2014).
10. Malhi, Y. & Wright, J. Spatial patterns and recent trends in the climate of tropical rainforest regions. *Phil. Trans. R. Soc. Lond. B* **359**, 311–329 (2004).
11. Asefi-Najafabady, S. & Saatchi, S. Response of African humid tropical forests to recent rainfall anomalies. *Phil. Trans. R. Soc. B* **368**, 20120306 (2013).
12. Adams, J. The distribution and variety of equatorial rain forest. <http://www.esd.ornl.gov/projects/qen/rainfo.html> (1998).
13. Ashton, M. S., Tyrrell, M. L., Spalding, D. & Gentry, B. (eds) *Managing Forest Carbon in a Changing Climate* (Springer, 2012).
14. Fauset, S. *et al.* Drought-induced shifts in the floristic and functional composition of tropical forests in Ghana. *Ecol. Lett.* **15**, 1120–1129 (2012).
15. Huete, A. *et al.* Overview of the radiometric and biophysical performance of the MODIS vegetation indices. *Remote Sens. Environ.* **83**, 195–213 (2002).
16. Myneni, R. B., Hall, F. G., Sellers, P. J. & Marshak, A. L. The meaning of spectral vegetation indices. *IEEE Trans. Geosci. Remote Sens.* **33**, 481–486 (1995).
17. Huete, A. R. *et al.* Amazon rainforests green-up with sunlight in dry season. *Geophys. Res. Lett.* **33**, L06405 (2006).
18. Nemani, R. R. *et al.* Climate-driven increases in global terrestrial net primary production from 1982 to 1999. *Science* **300**, 1560–1563 (2003).
19. de Wasseige, C., Bastin, D. & Defourny, P. Seasonal variation of tropical forest LAI based on field measurements in Central African Republic. *Agric. For. Meteorol.* **119**, 181–194 (2003).
20. Schneider, U. *et al.* GPCP's new land surface precipitation climatology based on quality-controlled in situ data and its role in quantifying the global water cycle. *Theor. Appl. Climatol.* **115**, 15–40 (2014).
21. Adler, R. F. *et al.* The Version 2 Global Precipitation Climatology Project (GPCP) monthly precipitation analysis (1979–present). *J. Hydrometeorol.* **4**, 1147–1167 (2003).
22. Huffman, G. J. *et al.* The TRMM Multi-satellite Precipitation Analysis: quasi-global, multi-year, combined-sensor precipitation estimates at fine scale. *J. Hydrometeorol.* **8**, 38–55 (2007).
23. Crowley, J. W., Mitrovica, J. X., Bailey, R. C., Tamisiea, M. E. & Davis, J. L. Land water storage within the Congo Basin inferred from GRACE satellite gravity data. *Geophys. Res. Lett.* **33**, L19402 (2006).
24. Reager, J. T. & Famiglietti, J. S. Characteristic mega-basin water storage behavior using GRACE. *Wat. Resour. Res.* **49**, (2013).
25. Liu, Y. Y., van Dijk, A. I. J. M., McCabe, M. F., Evans, J. P. & de Jeu, R. A. M. Global vegetation biomass change (1988–2008) and attribution to environmental and human drivers. *Glob. Ecol. Biogeogr.* **22**, 692–705 (2013).
26. Andela, N., Liu, Y. Y., van Dijk, A. I. J. M., de Jeu, R. A. M. & McVicar, T. R. Global changes in dryland vegetation dynamics (1988–2008) assessed by satellite remote sensing: comparing a new passive microwave vegetation density record with reflective greenness data. *Biogeosciences* **10**, 6657–6676 (2013).
27. Lucht, W., Schaphoff, S., Erbrect, T., Heyder, U. & Cramer, W. Terrestrial vegetation redistribution and carbon balance under climate change. *Carbon Balance Manag.* **1**, 6 (2006).
28. Lee, H. *et al.* Characterization of terrestrial water dynamics in the Congo Basin using GRACE and satellite radar altimetry. *Remote Sens. Environ.* **115**, 3530–3538 (2011).
29. Valentini, R. *et al.* The full greenhouse gases budget of Africa: synthesis, uncertainties and vulnerabilities. *Biogeosci. Discuss.* **10**, 8343–8413 (2013).
30. Nepstad, D. C., Tohver, I. M., Ray, D., Moutinho, P. & Cardinot, G. Mortality of large trees and lianas following experimental drought in an amazon forest. *Ecology* **88**, 2259–2269 (2007).

**Supplementary Information** is available in the online version of the paper.

**Acknowledgements** This study was supported by the NOAA NESDIS project (NA11NES4400010) and by the startup funds provided by the University at Albany, State University of New York. R.B.M. was funded by NASA's Earth Science Division. The views, opinions, and findings contained in this report are those of the authors and should not be construed as an official NOAA or US Government position, policy, or decision. H.C. is supported by the National Natural Science Foundation of China (grant number 41230422).

**Author Contributions** L.Z. and Y.T. contributed the central idea, analysed most of the data, and wrote the initial draft of the paper. The remaining authors contributed to refining the ideas, carrying out additional analyses and finalizing this paper.

**Author Information** Reprints and permissions information is available at [www.nature.com/reprints](http://www.nature.com/reprints). The authors declare no competing financial interests. Readers are welcome to comment on the online version of the paper. Correspondence and requests for materials should be addressed to L.Z. ([lzhou@albany.edu](mailto:lzhou@albany.edu)).

## METHODS

**Data.** This research analyses a variety of climate and vegetation data from ground observations and several independent satellite sensors (optical, thermal, passive and active microwave and gravity) over the Congo basin. We use (1) rainfall, terrestrial water storage (TWS), aerosol optical thickness (AOT), cloud optical thickness (COT), photosynthetically active radiation (PAR) and land surface temperature (LST) as climate drivers; and (2) enhanced vegetation index (EVI), normalized difference vegetation index (NDVI), vegetation optical depth (VOD) and canopy backscatter anomaly (CBA) as vegetation variables. Unlike optical and thermal remote sensing products (for example, NDVI, EVI and LST), microwave retrievals (for example, VOD and CBA) are not affected by atmospheric cloud cover and aerosol conditions. The low energy of microwave emission does, however, require a larger footprint, resulting in a relatively coarser spatial resolution of the microwave data than the optical and thermal data used in this study. The gravity sensors from the Gravity Recovery and Climate Experiment (GRACE) map the Earth's gravity fields by making accurate measurements of the distance between the two satellites and thus provide information about the distribution and flow of water mass within the Earth and its surroundings.

**MODIS data.** We use the globally validated Collection 5 MODerate resolution Imaging Spectroradiometer (MODIS) products of EVI<sup>15</sup> and NDVI<sup>15</sup> (monthly, 2000–2012), LST<sup>31</sup> (monthly, 2003–2012) and land cover and percentage vegetation cover<sup>32,33</sup> (yearly, 2001–2012) at 0.05° spatial resolution, and AOT<sup>34,35</sup> and COT<sup>34,36</sup> at 1° resolution (monthly, 2000–2012). The NDVI and EVI (MOD13C2), LST (MYD11C3), and land cover (MCD12C1) data were obtained from [https://lpdaac.usgs.gov/get\\_data](https://lpdaac.usgs.gov/get_data). The AOT and COT data (MOD08M3) were obtained from <http://ladsweb.nascom.nasa.gov/data/search.html>.

The MODIS EVI data (MOD13C2) are used primarily because EVI is more sensitive to dense forests than other vegetation indices such as NDVI and has been used widely in recent studies on tropical rainforests<sup>4–7</sup>. The MODIS EVI algorithm<sup>15</sup> uses the MODIS surface reflectance data in the blue, red and near-infrared spectral bands (which are corrected for molecular scattering, ozone absorption and aerosols) as its input. The blue band removes residual atmospheric contamination caused by smoke and sub-pixel thin clouds. A feedback adjustment is used to minimize canopy background variations and to enhance its sensitivity from sparse vegetation to very dense forests<sup>15,17</sup>. When properly filtered to remove atmospheric aerosol and cloud effects, the MODIS EVI data do not saturate, even over dense forests, and correlate well with leaf area, leaf biomass, canopy chlorophyll content, canopy photosynthetic activity and primary productivity<sup>16–18</sup>. The gridded EVI data sets include pixel-level quality assurance flags together with statistics of the EVI quality and input data. MOD13C2 represents the best retrievals possible from cloud-free high-quality spatial composites of the gridded 16-day 1-km EVI product (MOD13A2) at local solar time ~10:30 for the period 2000–2012 from the Terra satellite. It incorporates a quality assurance filter scheme that removes lower-quality and cloud-contaminated pixels during spatial aggregation. The accuracy of the MODIS EVI has been assessed over a widely distributed set of locations and time periods via validation efforts, with an error of  $\pm 0.01$  (ref. 7). The MODIS NDVI, which was calculated and processed similarly to the EVI by the same MODIS algorithm<sup>15</sup>, is used to assess the sun-view angle effects (see Supplementary Information).

The MODIS daytime LST<sup>31</sup> (MYD11C3) at local solar time ~13:30 for the period 2003–2012 from the Aqua satellite is used to quantify LST variations related to changes in vegetation and other land surface properties. Satellite-derived LST measures the temperature of the Earth's surface thermal emission. It is closely related to vegetation density/type and hence has been used to monitor deforestation and land cover change<sup>37,38</sup>. The MODIS LST has four measurements from the Terra and Aqua satellites. Here we choose the daytime Aqua observations because the LST contrast between vegetation and non-vegetation is expected to be strongest at ~13:30 than the other three MODIS measurements. However, it may have larger uncertainties than the other three measurements because clouds are more often seen over land during the afternoon than in the morning.

The MODIS land cover map<sup>32,33</sup> (MCD12C1) is available from 2001 and 2012 and can be used to identify and quantify large-scale changes in vegetation type and percentage vegetation cover. It provides a suite of land cover types by mapping global land cover using spectral and temporal information derived from MODIS using a supervised decision-tree classification method based on a database of high-quality land cover training sites<sup>32</sup>.

The MODIS level 3 joint aerosol/water-vapour/cloud products<sup>34–36</sup> (MOD08M3) provide AOT and COT data collected from the Terra satellite for the period 2000–2012. We used the fields of *Optical\_Depth\_Land\_And\_Ocean\_Mean\_Mean*, which contains AOT at 0.55  $\mu\text{m}$  for both ocean (best) and land (corrected), and *Cloud\_Optical\_Thickness\_Combined\_Mean\_Mean*, which contains the monthly mean values of daily mean of combined COT (liquid plus ice), from the MOD08M3 product.

**Rainfall data.** We use three gridded monthly rainfall data sets from the Global Precipitation Climatology Centre (GPCC)<sup>20</sup> at 1° resolution (1950–2012), the Global

Precipitation Climatology Project (GPCP)<sup>21</sup> at 2.5° resolution (1979–2012) and the Tropical Rainfall Measuring Mission (TRMM) and other satellites<sup>22</sup> at 0.25° resolution (1998–2012). The GPCC data provides the GPCC's most accurate *in situ* land surface precipitation analysis product by combining the Full Data V6 Product (1901–2010), based on quality-controlled data from 67,200 stations worldwide that feature record durations of ten years or longer, with the V4 monitoring product (2011–2012), based on quality-controlled data from 7,000 stations. The GPCP version 2.2 data provides combined gauge measurements and satellite-derived precipitation by taking advantages of the strengths of each of several sources into a final merged product. The 3B43 version 7 TRMM data provides the best-estimate precipitation rate and root-mean-square precipitation-error estimates by combining four independent precipitation fields. Despite their differences in data source, duration, spatial resolution and processing, these three rainfall data sets show similar and consistent rainfall variability during April–May–June over the study region (Fig. 1). GPCC and TRMM have higher spatial resolution and thus are mostly used in our analysis. We use the former (1950–2012) to examine the long-term variability of rainfall and the latter (2000–2012) to examine spatial patterns of rainfall in the last 13 years. The data sets were obtained from <http://www.esrl.noaa.gov/psd/>, <http://www.esrl.noaa.gov/psd/data/gridded/data.gpcp.html> and [http://mirador.gsfc.nasa.gov/collections/TRMM\\_3B43\\_007.shtml](http://mirador.gsfc.nasa.gov/collections/TRMM_3B43_007.shtml), respectively.

We had previously planned to include the gridded Climatic Research Unit (CRU) rainfall data<sup>39</sup> (CRU\_TS\_3.21) for the period 1950–2012 in our analysis as well. However, we found that the data of CRU differed from those of GPCC, GPCP and TRMM in the last decade over our study region owing to the insufficient ground observations used in the CRU. Asefi-Najafabady and Saatchi<sup>11</sup> also compared the rainfall quality of CRU and TRMM and found large uncertainties in CRU over the African forests for the period after 1990 owing to paucity of station data, whereas the TRMM products have relatively low bias in magnitude and errors in capturing rainfall spatial patterns.

**TWS data.** We use the gridded monthly Release 05 (RL05) TWS data from GRACE<sup>23,40,41</sup> at 1° resolution (2003–2012). It has three products, processed by the University of Texas' Center for Space Research, NASA's Jet Propulsion Laboratory and Germany's GeoForschungsZentrum, and was obtained from <http://grace.jpl.nasa.gov/data/gracemonthlymassgridsland/>. TWS represents the total water storage changes in wetlands, rivers, ground water, soil moisture and wet biomass in terms of anomalies relative to a mean total storage value. It is determined by the balance between source (precipitation) and sink (runoff, evapotranspiration) terms, and so a change in either source or sink will change TWS<sup>23,24</sup>. Although two areas may receive similar amounts of precipitation, the resulting storage response may differ owing to differences in temperature and the characteristics of land surface properties (for example, vegetation type/amount, soil depth and porosity, and topography) with which the water interacts<sup>24</sup>. Given that a 200-km-wide Gaussian filter was applied to the data, TWS quantifies a large-scale and low-frequency signal of TWS anomalies. The year-to-year TWS values from the University of Texas' Center for Space Research and NASA's Jet Propulsion Laboratory are similar but differ slightly from those from Germany's GeoForschungsZentrum (Fig. 3c and Extended Data Fig. 2). Our understanding and validation of TWS products are insufficient for a precise assessment of the quality among these three data sets, so here we simply use the ensemble-mean TWS with equal weights to illustrate the spatial pattern of TWS trends (Fig. 2e). Nevertheless, the results from the three data sets generally show similar decreasing trends in spatial patterns (Fig. 2e and Extended Data Fig. 2) and interannual variations at the regional level (Fig. 3b).

**Radiation data.** We use gridded monthly data of downward PAR at the surface from Clouds and Earth's Radiant Energy System (CERES)<sup>42</sup> at 1° resolution (2003–2012). The CERES products contain monthly mean direct and diffuse surface fluxes (CERES\_SYN1deg\_Ed3A) of PAR under all-sky and clear-sky conditions, which were obtained from <http://ceres.larc.nasa.gov/>. The total incident all-sky PAR was calculated by summarizing direct and diffuse PAR fluxes. The total incident shortwave radiation shows changes similar to PAR's but with a larger magnitude (not shown for brevity).

**VOD data.** We use gridded monthly VOD data retrieved from the Special Sensor Microwave Imager (SSM/I) and the Advanced Microwave Scanning Radiometer—Earth Observing System (AMSR-E)<sup>25</sup> at 0.25° resolution. VOD is a radiometric parameter retrieved from passive microwave satellite observations which can penetrate deeper into the canopy than can optical remotely sensed data such as EVI and is directly proportional to total vegetation water content in all the aboveground biomass, including both woody and leafy components<sup>43–45</sup>. Unlike EVI, VOD is sensitive to water rather than chlorophyll and hence to both photosynthetic and non-photosynthetic aboveground biomass<sup>46,47</sup>. The VOD retrievals from the SSM/I (January 1988–June 2002) and AMSR-E (July 2002–December 2010) sensors<sup>25</sup> were merged to create a single continuous long-term time series by using a cumulative distribution frequency matching technique<sup>48–50</sup>. Because of its higher retrieval accuracy, the AMSR-E VOD was selected as the reference with which to adjust the SSM/I

data. We note that the merging process has little influence on the long-term trends, that is, the trends from their original sources are kept unchanged. A comprehensive study has demonstrated that this long-term VOD data set is able to monitor global changes in total aboveground vegetation water content and biomass over various land cover types from grasslands to tropical forests<sup>25</sup>. The AMSR-E sensor stopped working in October 2011, which limits our analysis up to 2010.

**CBA data.** We also use gridded CBA of the SeaWinds scatterometer data onboard Quick Scatterometer (QSCAT)<sup>11</sup> (2000–2009) at 0.04° resolution. CBA provides a reliable remote sensing technique to monitor the impact of climate on tropical forests, especially in detecting large-scale tree mortality and tree leaf abscission. QSCAT is an active radar sensor operating at microwave frequency (13.4 GHz) and provides daily (6.00 and 18.00) measurements of the backscatter signal from forest canopies. QSCAT backscatter measurements over dense tropical forests are sensitive only to the top canopy structure and moisture and contain little information about the underlying soil moisture. The global wall-to-wall acquisition of QSCAT data stopped in November 2009, limiting our analysis up to 2009.

**Data processing.** The African rainforests span the equatorial region by nearly seven degrees from north to south, but some forested regions such as in West Africa have extensive cloud and aerosol contaminations, as can be inferred from optical remote products such as MODIS NDVI and EVI. We chose our study region and study period after carefully assessing the EVI data quality (Extended Data Fig. 1). First, the MODIS land cover classification and percentage forest cover data were used to define intact forest canopies in the Congo basin. Only forested pixels at 0.05° resolution that have a forest cover exceeding 80% and have no land cover/use change detected during the period 2001–2012 are considered. Second, the quality assurance flags of each monthly EVI composite were checked to count the total number of high-quality EVI composites on every pixel at 0.05° resolution for the 13-year period. A high-quality EVI composite was defined as one without the presence of clouds (adjacent clouds, mixed clouds and shadows) and aerosol loadings that typically corrupt EVI (climatology and high aerosols)<sup>6</sup>. The three-month period of April–May–June shows the highest percentage of high-quality EVI pixels (or the least contamination of aerosols and clouds) over the 13-year period and also coincide with the first peak season of EVI and rainfall, so we focus our study period on April–May–June only. Third, the quality assurance statistics were used to create a high-quality EVI mask at 0.05° resolution. The masked pixels contain only those pixels having at least 80% of monthly composites in April–May–June (or at least 31 of the total 39 monthly composites) for the 13-year study period, which represent at least ten years of high-quality data. Only the masked high-quality pixels are considered so that the same group of EVI pixels is analysed for the entire study period. Fourth, for each of the masked pixels, a monthly high-quality EVI anomaly time series in April–May–June was first created by removing the monthly high-quality EVI climatology for the period 2000–2012 and then aggregated into one single April–May–June high-quality EVI anomaly image for each year. Fifth, the 0.05° April–May–June high-quality anomaly images were spatially aggregated into coarser resolution images at 0.25° to enhance the pixel-level signal-to-noise ratio and also match the spatial resolution of TRMM rainfall. We only consider those 0.25° resolution pixels that (1) have at least five sub-pixels that are masked as high-quality at 0.05° resolution (to ensure adequate samples for spatial averaging) and (2) are defined as intact forested pixels in the first step. Some isolated pixels near the border of enclosed forests were removed from the 0.25° mask map to minimize human impacts. The above steps lead to the choice of our study region over only the intact forest pixels with high-quality EVIs (5°N–6°S, 14°E–31°E) over the Congo basin, which in total consists of 1,438 pixels at 0.25° resolution (Extended Data Fig. 1).

Like the MODIS EVI, the data of rainfall, NDVI, LST, TWS, AOT, COT, PAR, VOD and CBA at different spatial resolutions were temporally averaged into anomalies in April–May–June and other seasons and then re-projected into our study region at 0.25° resolution. For the data with a spatial resolution coarser than 0.25°, nearest-neighbour interpolation was used. Regional and spatial aggregations were applied only over the masked 0.25° pixels where the MODIS data has the most high-quality EVI composites.

The VOD data can provide complementary information on vegetation dynamics when compared to other satellite products<sup>25,26</sup> and especially it can be used to monitor global vegetation biomass change over various land cover types<sup>25</sup>. However, as a new product, the VOD has not been validated against ground observations. For example, we found that there are few strong VOD anomalies with a value exceeding 0.2 or less than -0.2 (or 20% of the absolute regional mean VOD value) at local scales, which represent 0.04% of all the data, possibly owing to uncertainties and errors from measurements and retrievals or local fires. Instead of excluding these values, which would create missing data, we treat them as local-scale noise. We use empirical orthogonal function (EOF) analysis to isolate the VOD variance associated with the smaller scales. The EOF method has been extensively used to analyse the spatial and temporal variability of geophysical fields by decomposing the

data into a set of spatial patterns of variability (referred to as EOF modes) and corresponding time variations (referred to as EOF time series)<sup>51,52</sup>. Its goal is to express the signal in terms of a relatively small number of EOFs to describe as much of the original information as possible. The EOF modes show the spatial structure of the major factors that can account for the temporal variations, which represent spatial variability. The EOF time series tells us how the amplitude of each EOF mode varies with time. The first few EOFs contain the majority of data variance and the highest spatial coherence and the last few EOFs are noise-dominated and have the least variance. Therefore, the inversion of the EOF transform using only the first few EOFs provides a noise-filtered data set. We used the first 12 EOFs to restructure the VOD data, which explains 90% of the data variance. The restructured VOD looked almost identical to the original data, except for the smoothing of few strong VOD anomalies.

**Quantification of temporal changes.** When choosing methods with which to quantify the temporal changes in EVI and other variables we should consider how rainfall changes with time in our study region. Unlike short-term and intense droughts that have recently occurred in the Amazon forests<sup>4–8</sup>, the African forests have experienced a long-term and gradual rainfall reduction<sup>10,11</sup>. The effects of such rainfall changes on vegetation are more complex than short-term droughts because forest composition and structure may change over time<sup>1,2,14</sup>. So we expect to see small and gradual changes in moisture properties (and, hence, vegetation), instead of large-scale tree mortality similar to what has occurred in the Amazon<sup>8</sup>.

Here we use two simple methods to quantify the gradual temporal change in a variable  $y(t)$ , which represents EVI or any other variables over time  $t$ . The first method is to calculate the differences in the mean values of  $y(t)$  between two individual periods. The two periods are defined as the last and first three years if the data record is less than 20 years. Otherwise, we use the last and first decades. The first method is straightforward and effective if  $y(t)$  contains a deterministic trend, but the resulting change depends on the chosen time periods if  $y(t)$  has strong interannual variations. The second method is to estimate the linear time trend of  $y(t)$  using ordinary least squares over a certain time period (that is, the estimated change per decade). Although most of the remotely sensed data are only available for 10–13 years, the second method can be a good indicator if  $y(t)$  shows a persistent trend (either upward or downward) with time. In particular, it can provide the  $P$  value of the Student's  $t$  statistic that quantifies the probability of whether the estimated trend is statistically significantly different from zero or simply due to random noise. Nevertheless, both methods should provide consistent results if there is a persistent trend in the data as shown in most of the variables in our analysis.

Both methods were used for time series analysis in our study, but the first method was not used in the spatial pattern analysis because the pixel-level time series is noisier than the regional mean data. So we express the temporal change mostly as a linear trend—which is one simple way to quantify the gradual change while reducing year-to-year data noise. We do realize the limitation of estimating a linear trend for a short time series of 10–13 years for most of the satellite data. Hence, the estimated trend only applies to the study period and thus should not be extrapolated linearly over longer periods.

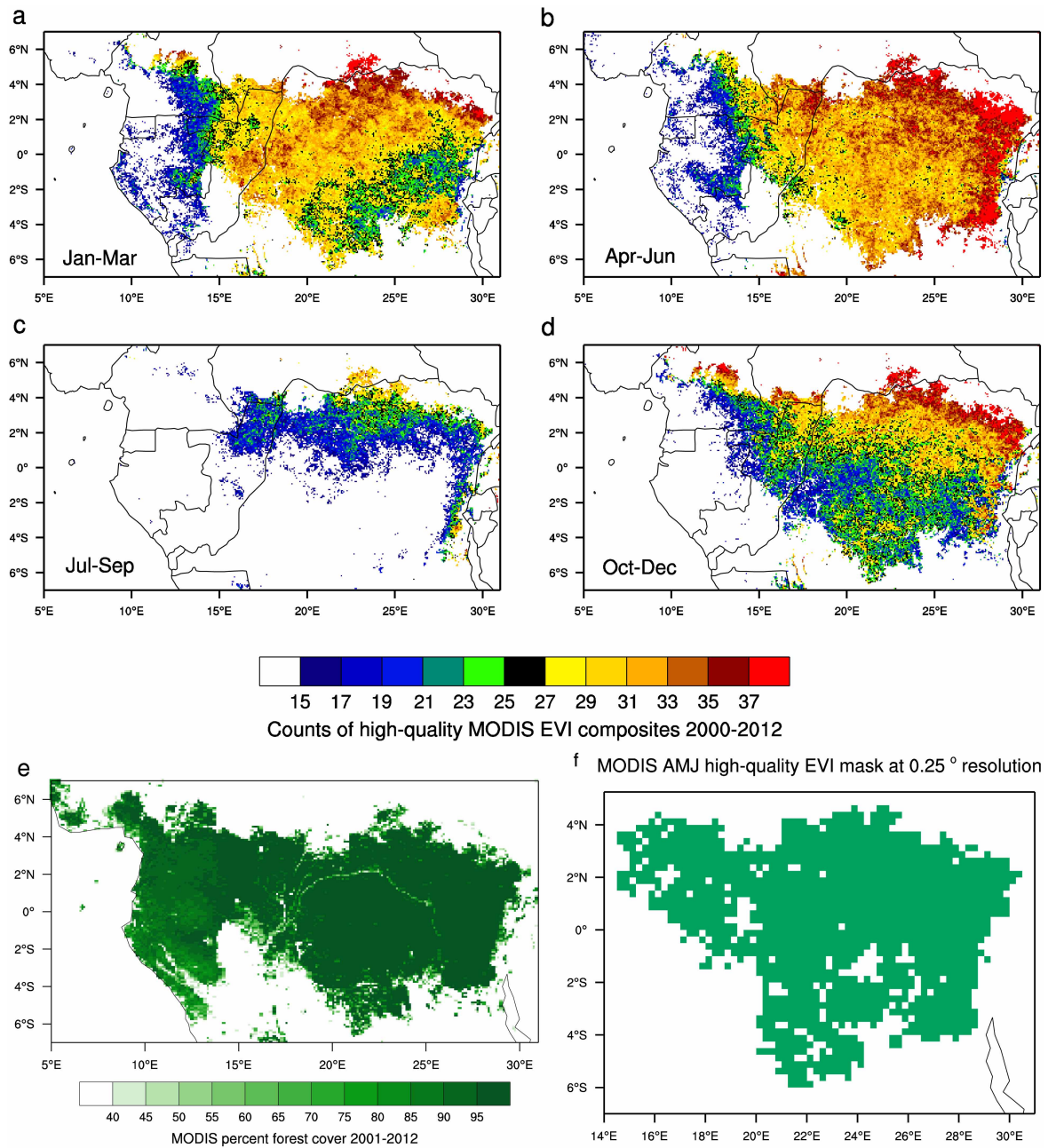
There is another method that has been used extensively to detect and quantify the drought impacts in studies of the Amazon rainforests and has proved to be very effective<sup>5–8</sup>. This method calculates the standardized anomaly for one particular drought year  $y(t_0)$  as the departure of  $y(t)$  from the climatological mean of  $y(t)$  and normalized by the standard deviation of  $y(t)$ , while the measurement from the particular drought year  $y(t_0)$  is excluded from the calculations of mean and standard deviation. It requires us to identify abnormal years versus normal years, which is relatively easy in the Amazon given the two historic drought events that occurred within the last 13 years. However, our study region has not experienced significant widespread droughts similar to what occurred in the Amazon<sup>8</sup>, and the drought-affected areas are smaller in spatial extent than the Amazon and vary by periods<sup>1</sup>. Also, the decreasing trend in EVI and other variables often makes it difficult to define one particular year as an abnormal year because the last few years always have lower values than the first few years. Consequently, this method is not used in our analysis.

**Correlation analysis.** The linear correlation coefficient (Pearson's  $R$ ) was calculated between two time series to quantify their concurrent and lagged association. The significance level of correlation ( $P$  value) is estimated using a two-tailed Student's  $t$ -test. The null hypothesis is that the two variables used to calculate  $R$  are independent (that is,  $R = 0.0$ ).

The acronyms and abbreviations are listed in Supplementary Table 4.

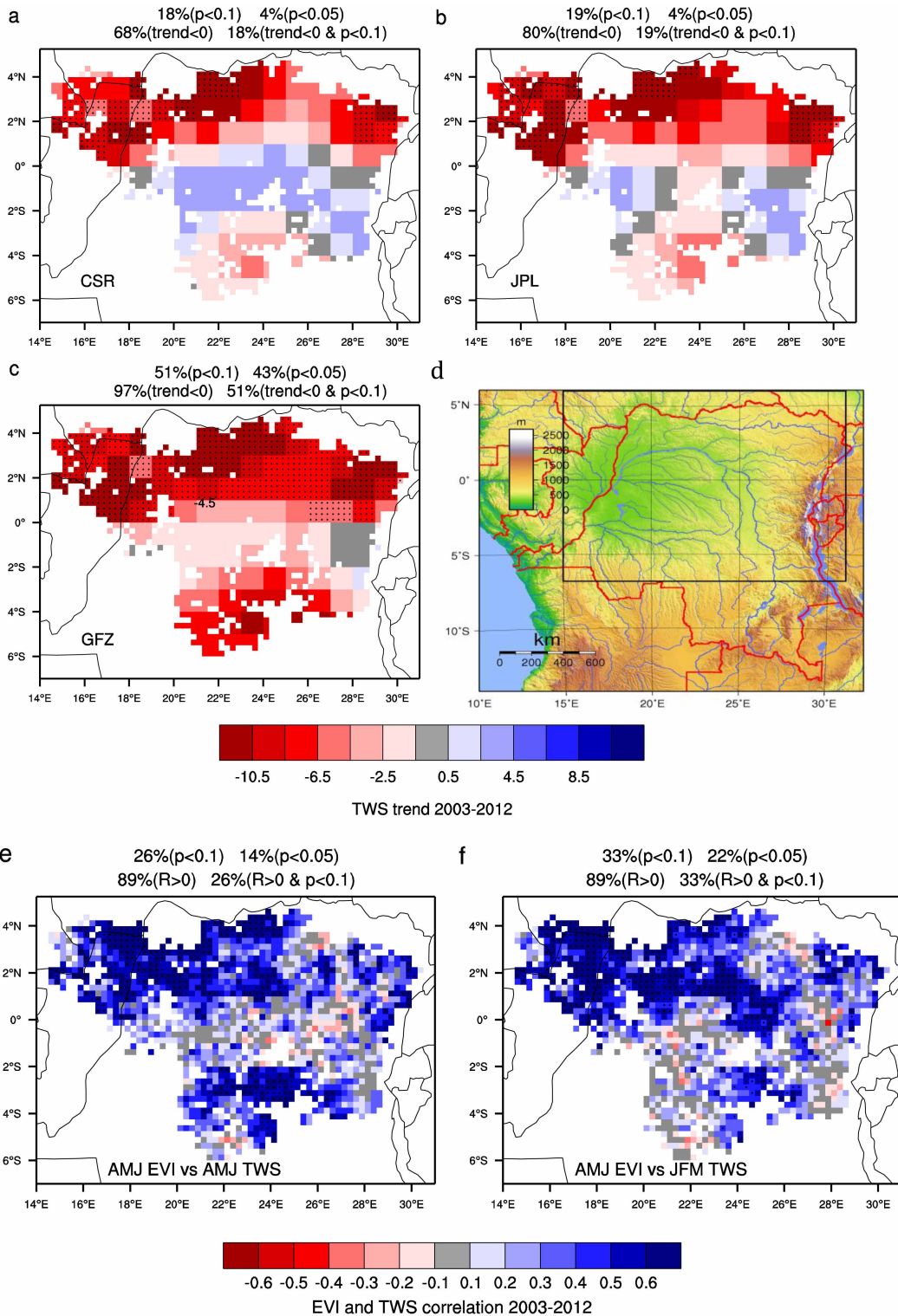
- Wan, Z. New refinements and validation of the MODIS land surface temperature/emissivity products. *Remote Sens. Environ.* **112**, 59–74 (2008).
- Friedl, M. A. *et al.* MODIS Collection 5 global land cover: algorithm refinements and characterization of new datasets. *Remote Sens. Environ.* **114**, 168–182 (2010).
- DiMiceli, C. M. *et al.* Annual Global Automated MODIS Vegetation Continuous Fields (MOD44B) at 250 m Spatial Resolution for Data Years Beginning Day 65, 2000–2010,

- Collection 5 Percent Tree Cover. (Univ. Maryland, 2011); <http://www.landcover.org/data/vcf>.
34. King, M. D. *et al.* Cloud and aerosol properties, precipitable water and profiles of temperature and water vapor from MODIS. *IEEE Trans. Geosci. Rem. Sens.* **41**, 442–458 (2003).
  35. Remer, L. A. *et al.* MODIS aerosol algorithm, products and validation. *J. Atmos. Sci.* **62**, 947–973 (2005).
  36. Platnick, S. *et al.* The MODIS cloud products: algorithms and examples from Terra. *IEEE Trans. Geosci. Rem. Sens.* **41**, 459–473 (2003).
  37. Hansen, M. C. *et al.* A method for integrating MODIS and Landsat data for systematic monitoring of forest cover and change in the Congo Basin. *Remote Sens. Environ.* **112**, 2495–2513 (2008).
  38. van Leeuwen, T. T. *et al.* Optimal use of land surface temperature data to detect changes in tropical forest cover. *J. Geophys. Res.* **116**, G02002 (2011).
  39. Harris, I., Jones, P. D., Osborn, T. J. & Lister, D. H. Updated high-resolution grids of monthly climatic observations. *Int. J. Climatol.* **34**, 623–642 (2013).
  40. Landerer, F. W. & Swenson, S. C. Accuracy of scaled GRACE terrestrial water storage estimates. *Water Resour. Res.* **48**, W04531 (2012).
  41. Swenson, S. C. & Wahr, J. Post-processing removal of correlated errors in GRACE data. *Geophys. Res. Lett.* **33**, L08402 (2006).
  42. Wielicki, B. A. *et al.* Clouds and the Earth's Radiant Energy System (CERES): an Earth observing system experiment. *Bull. Am. Meteorol. Soc.* **77**, 853–868 (1996).
  43. Kirdyashev, K. P., Chukhlantsev, A. A. & Shutko, A. M. Microwave radiation of the Earth's surface in the presence of a vegetation cover. *Radio Eng. Electron. Phys.* **24**, 37–44 (1979).
  44. Kerr, Y. H. & Njoku, E. G. A semiempirical model for interpreting microwave emission from semiarid land surfaces as seen from space. *IEEE Trans. Geosci. Remote Sens.* **28**, 384–393 (1990).
  45. Jackson, T. J. & Schmugge, T. J. Vegetation effects on the microwave emission of soils. *Remote Sens. Environ.* **36**, 203–212 (1991).
  46. Shi, J. C. *et al.* Microwave vegetation indices for short vegetation covers from satellite passive microwave sensor AMSR-E. *Remote Sens. Environ.* **112**, 4285–4300 (2008).
  47. Jones, M. O., Jones, L. A., Kimball, J. S. & McDonald, K. C. Satellite passive microwave remote sensing for monitoring global land surface phenology. *Remote Sens. Environ.* **115**, 1102–1114 (2011).
  48. Liu, Y. Y., de Jeu, R. A. M., McCabe, M. F., Evans, J. P. & van Dijk, A. I. J. M. Global long-term passive microwave satellite-based retrievals of vegetation optical depth. *Geophys. Res. Lett.* **38**, L18402 (2011).
  49. Liu, Y. Y. *et al.* Developing an improved soil moisture dataset by blending passive and active microwave satellite-based retrievals. *Hydrol. Earth Syst. Sci.* **15**, 425–436 (2011).
  50. Liu, Y. Y. *et al.* Trend-preserving blending of passive and active microwave soil moisture retrievals. *Remote Sens. Environ.* **123**, 280–297 (2012).
  51. Halldor, B. & Venegas, S. A. *A Manual for EOF and SVD Analyses of Climate Data.* (Report No. 97-1, Centre for Climate and Global Change Research, McGill Univ., 1997).
  52. Zhou, L., Tian, Y., Chen, H., Dai, Y. & Harris, R. A. Effects of topography on assessing wind farm impacts using MODIS data. *Earth Interact.* **17**, 1–18 (2013).



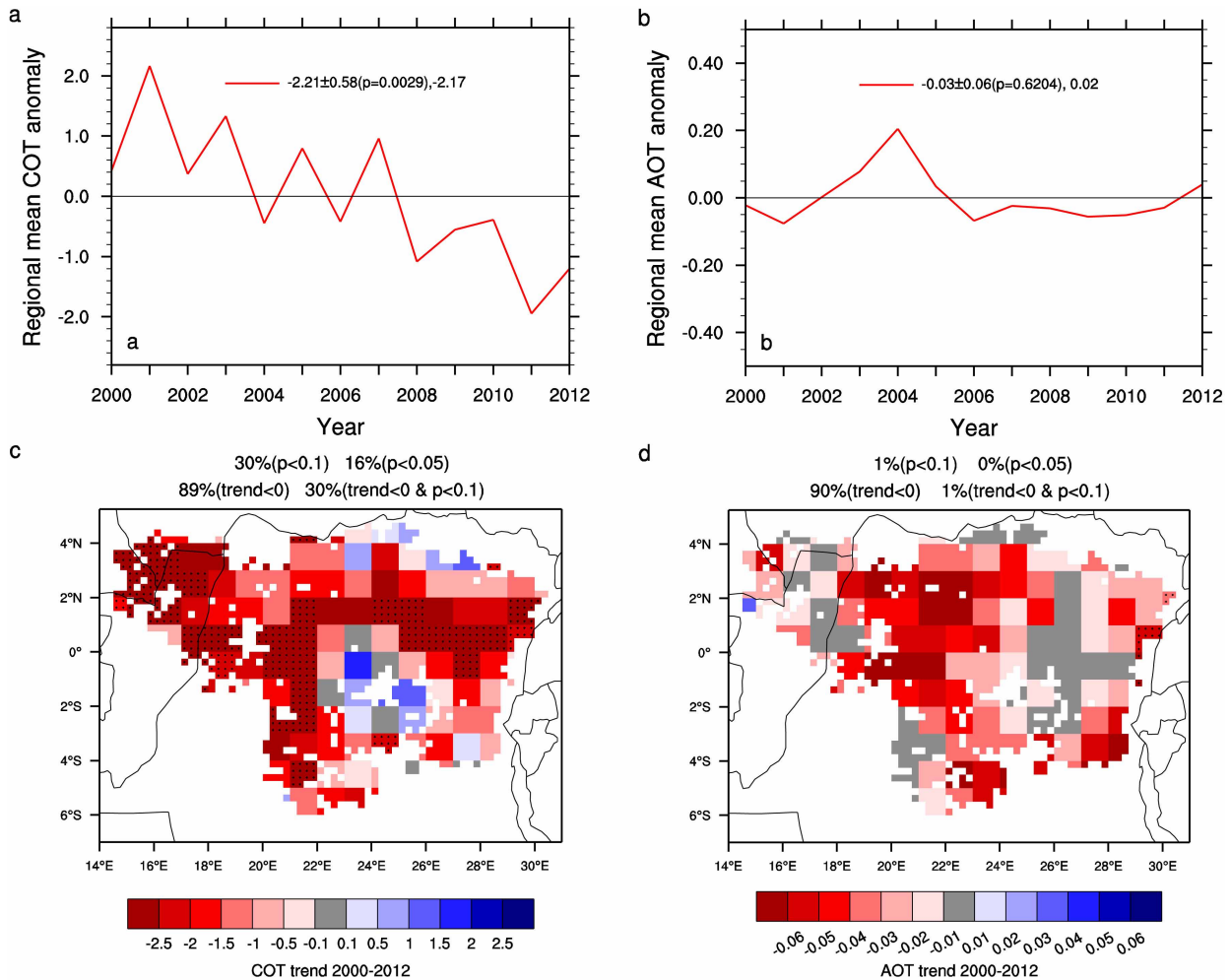
**Extended Data Figure 1 | Statistics of MODIS data quality and MODIS high-quality EVI mask.** **a–d**, Seasonal statistics of the total number of high-quality MODIS EVI composites over forested pixels at 0.05° resolution in central tropical Africa (7° S–7° N, 5–31° E) for the period 2000–2012. For each season, there are up to 39 EVI composites (three composites per year multiplied

by 13 years) for every pixel. **e**, The climatology of MODIS percentage forest cover at 0.05° resolution. **f**, The high-quality MODIS April–May–June EVI mask at 0.25° resolution over the intact Congo forest (6° S–5° N, 14–31° E) used in the analysis (see details in Methods).



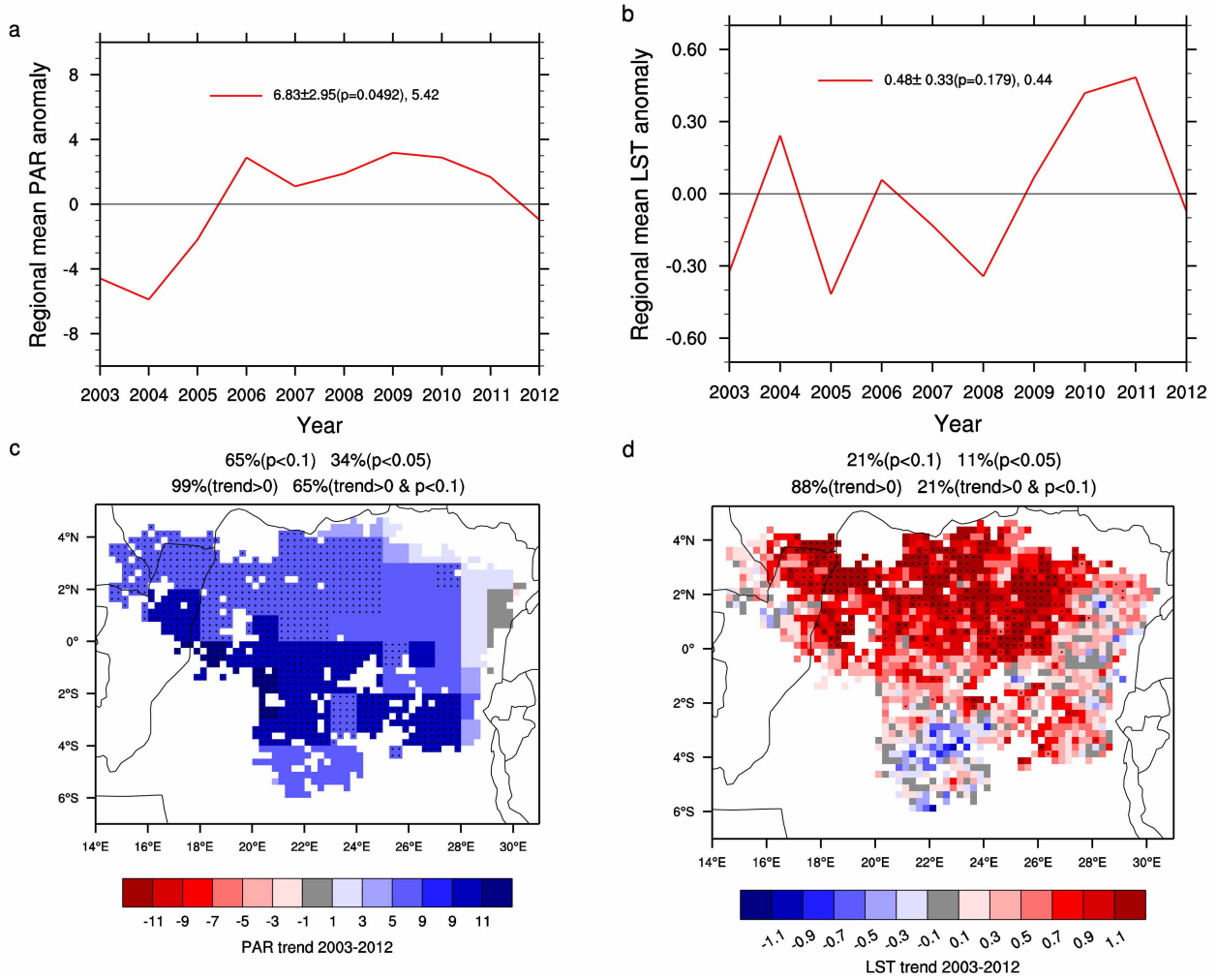
**Extended Data Figure 2 | Spatial patterns of linear trends in April–May–June TWS (cm per decade) and correlation coefficients  $R$  between TWS and EVI for the period 2003–2012.** a–c, As in Fig. 2e but for TWS from individual data processing centres (the University of Texas’ Center for Space Research (CSR), NASA’s Jet Propulsion Laboratory (JPL) and Germany’s GeoForschungsZentrum (GFZ)). d, The topography of the Congo basin ([http://en.wikipedia.org/wiki/File:Congo\\_Kinshasa\\_Topography.png](http://en.wikipedia.org/wiki/File:Congo_Kinshasa_Topography.png)).

e, f,  $R$  between April–May–June EVI and ensemble-mean TWS in April–May–June (AMJ) and January–February–March (JFM). The significance level of  $R$  (its  $P$  value) is estimated using a two-tailed Student’s  $t$ -test. Pixels with a plus symbol have a linear trend or an  $R$  that is statistically significant at  $P < 0.1$ . The percentages of pixels with trends or  $R$  at  $P < 0.05$  and  $P < 0.1$  and the percentages of pixels with negative trends or positive  $R$  over the study region are shown.

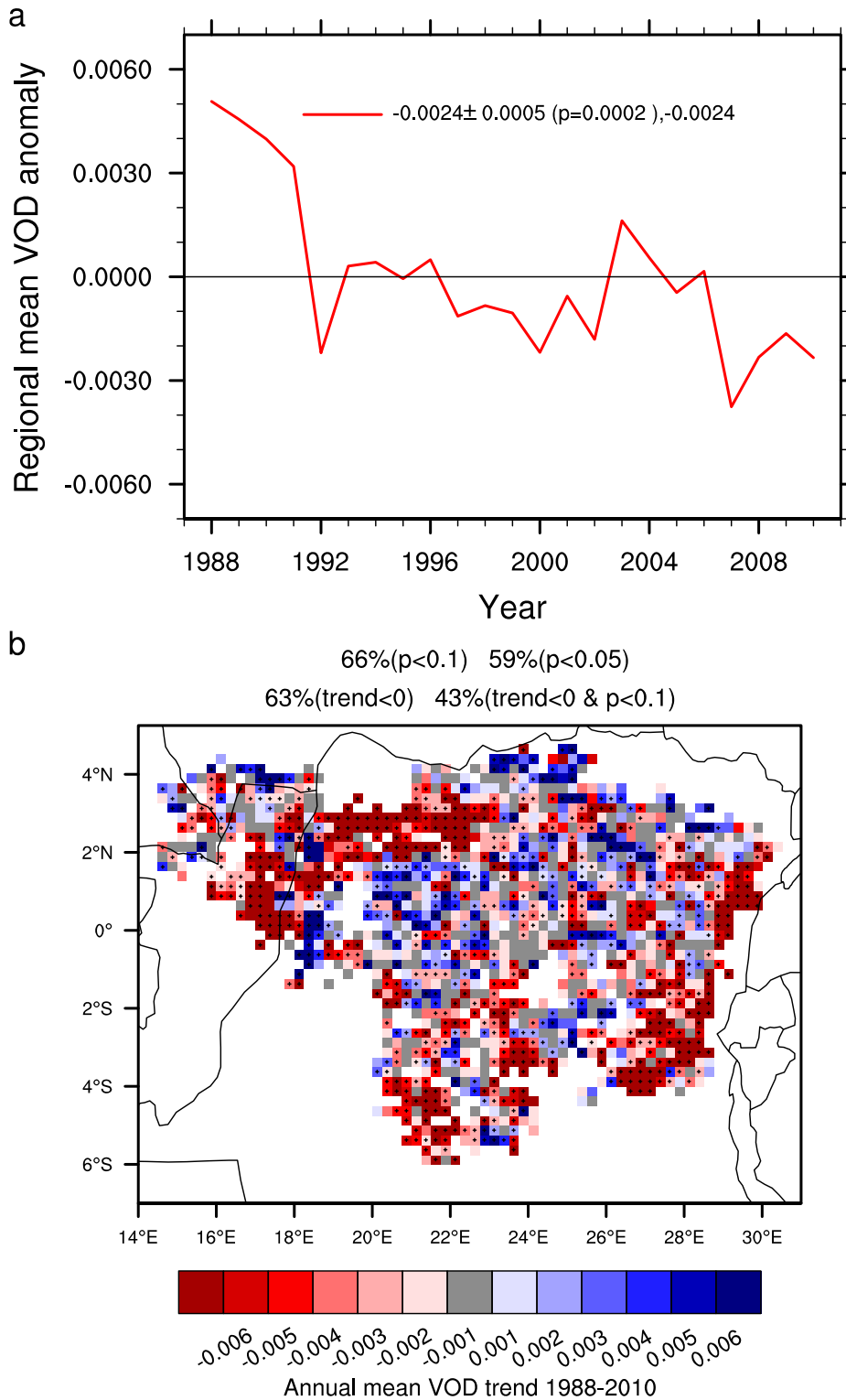


**Extended Data Figure 3 | Regional mean anomalies and linear trends per decade for COT and AOT (unitless) in April-May-June for the period 2000–2012. a, b, As in Fig. 3a. c, d, As in Fig. 2a. The dramatic AOT increase in**

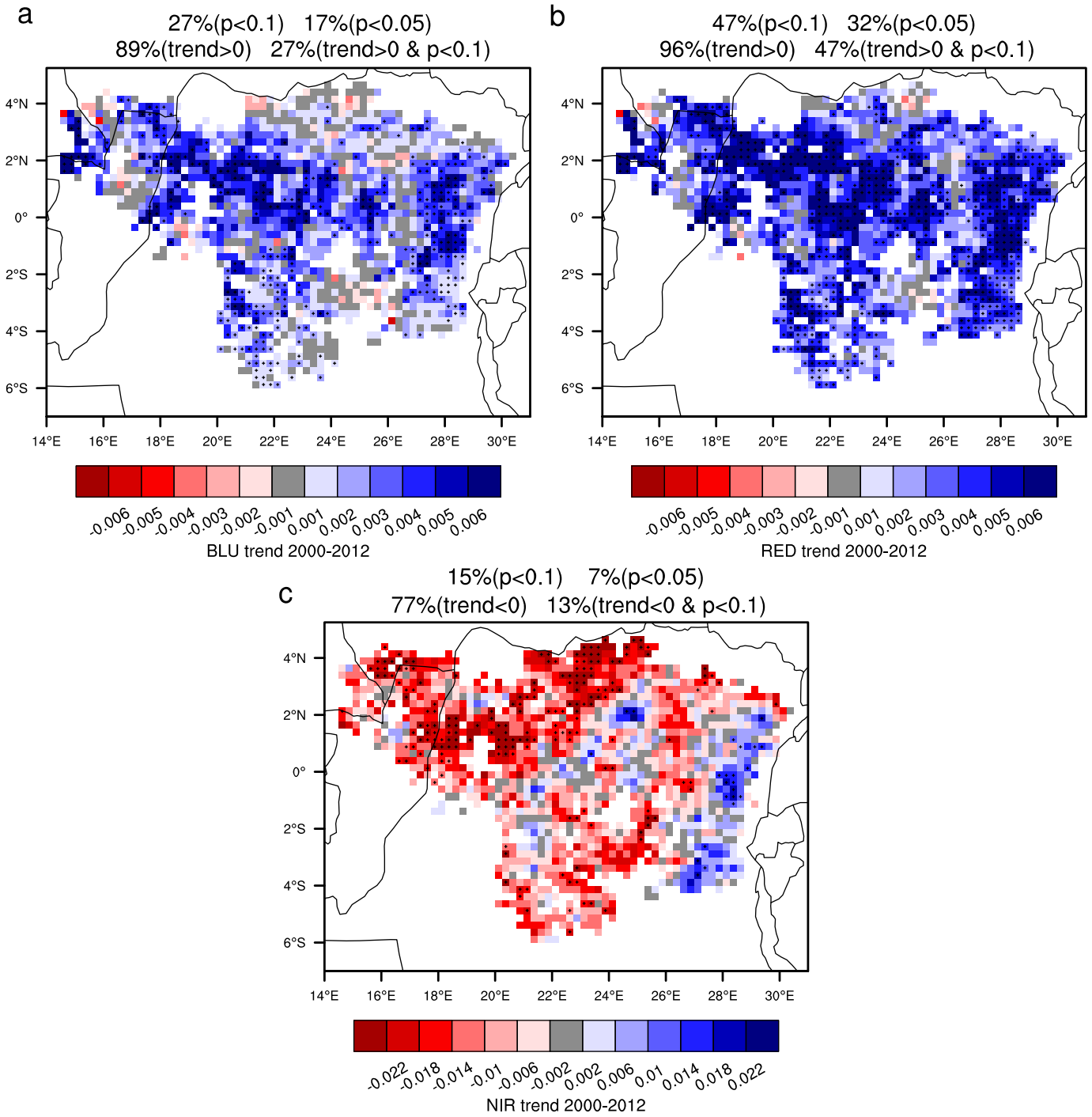
2004 is due to volcanic eruptions of the mountains Nyamulagira and Nyiragongo, which are located on the eastern border of the study region, on 25 May 2004. However, if the year 2004 is excluded, the AOT changes little.



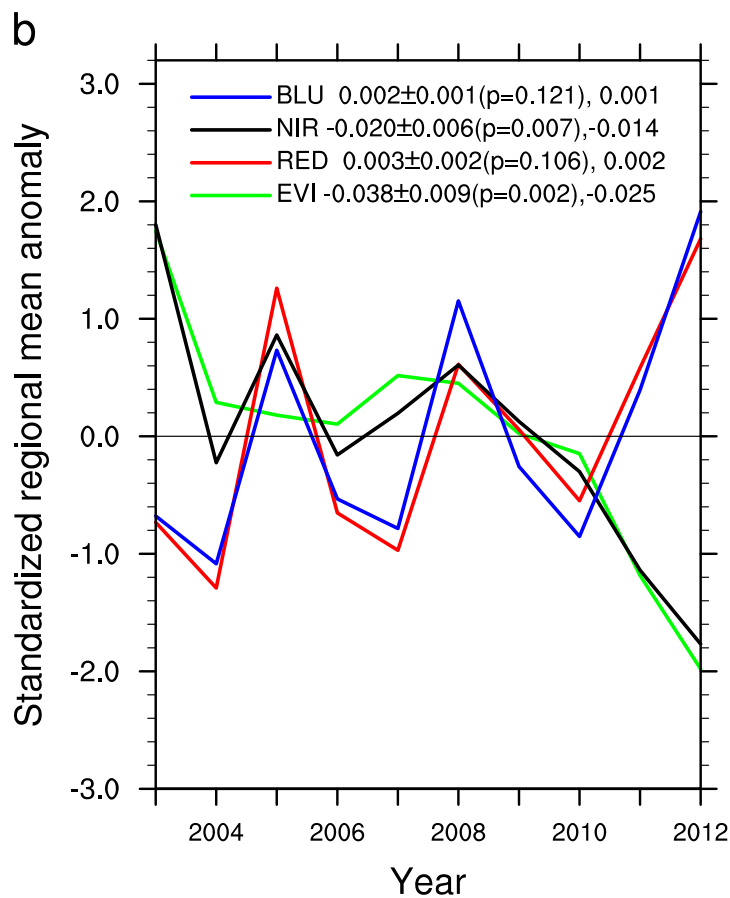
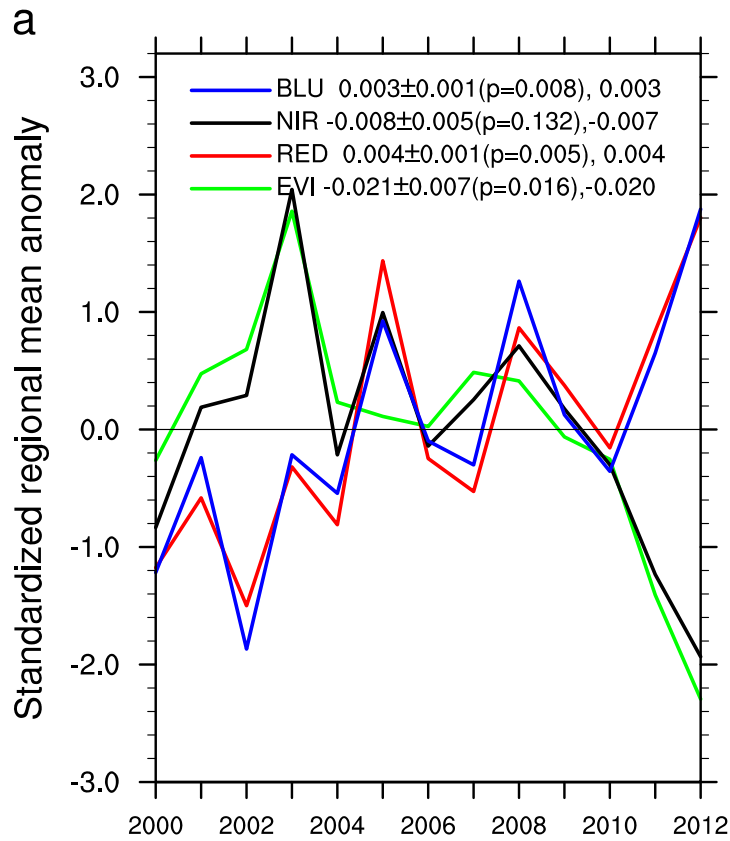
Extended Data Figure 4 | Regional mean anomalies and linear trends per decade for PAR and LST in April–May–June for the period 2003–2012. a, c, PAR ( $\text{W m}^{-2}$ ); b, d, LST ( $^{\circ}\text{C}$ ); a, b, as in Fig. 3c; c, d, as in Fig. 2b.



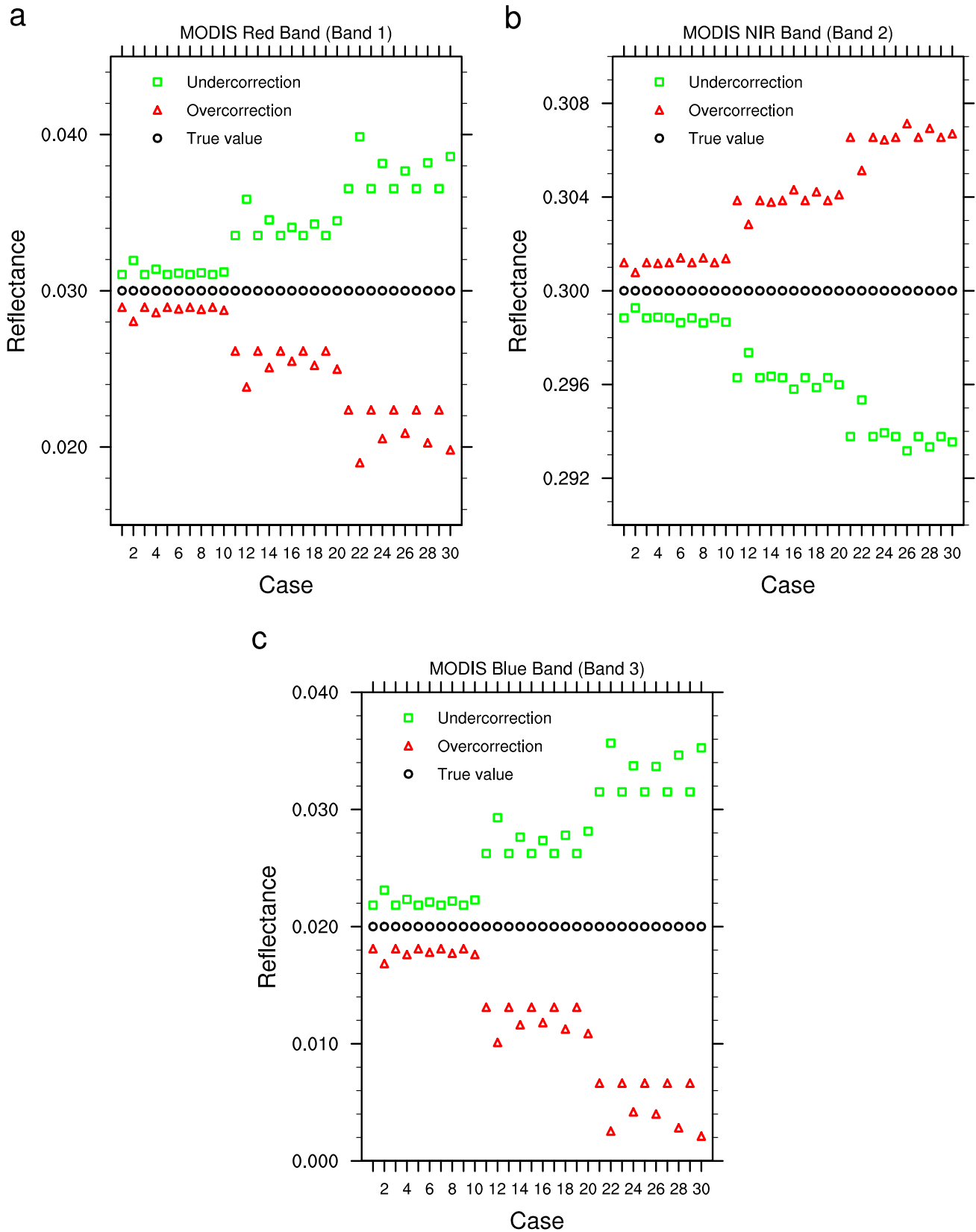
Extended Data Figure 5 | Annual mean VOD anomalies (unitless; a) and linear trends per decade (b). For the period 1988–2010 (as in Fig. 4).



Extended Data Figure 6 | Spatial patterns of linear trends per decade in April–May–June for MODIS reflectance in the blue (BLU; a), red (RED; b) and near-infrared (NIR; c) spectral bands. For the period 2000–2012 (as in Fig. 2a).

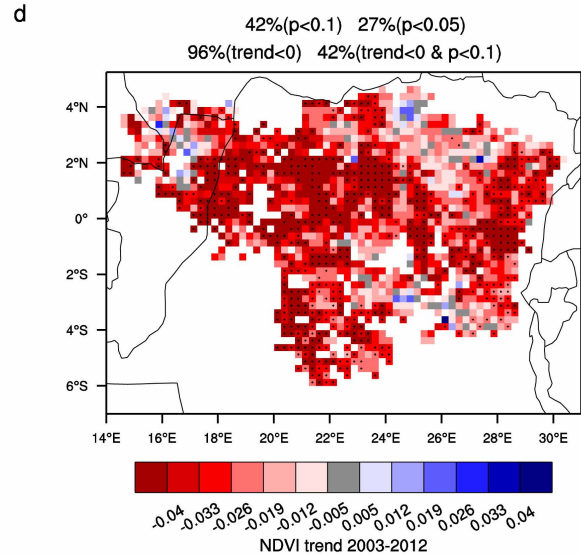
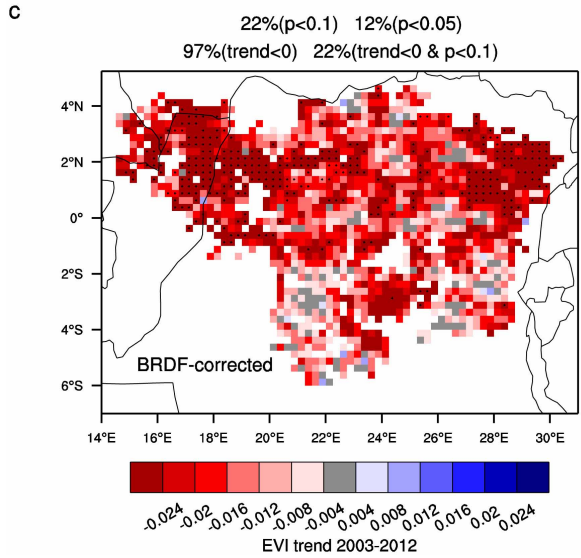
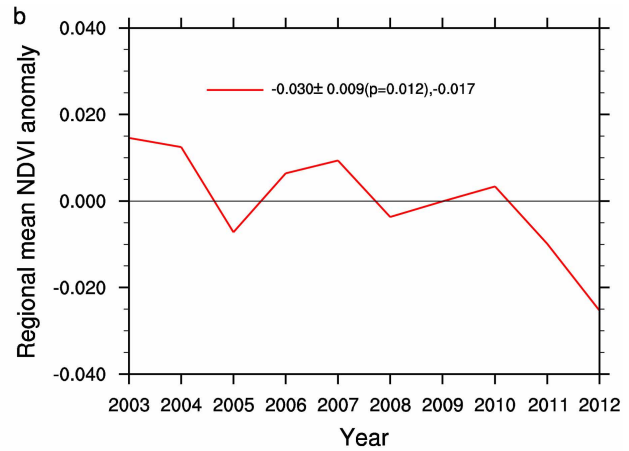
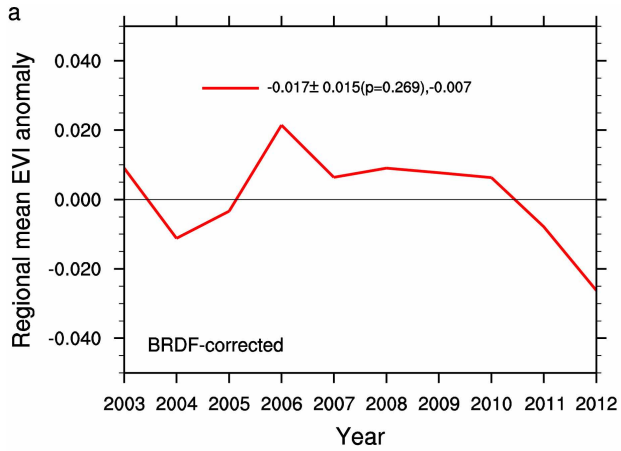


Extended Data Figure 7 | Regional mean anomalies for MODIS EVI and reflectance in the blue (BLU), red (RED) and near-infrared (NIR) spectral bands. For the period of 2000–2012 (a) (as in Fig. 3a) and 2003–2012 (b) (as in Fig. 3c).



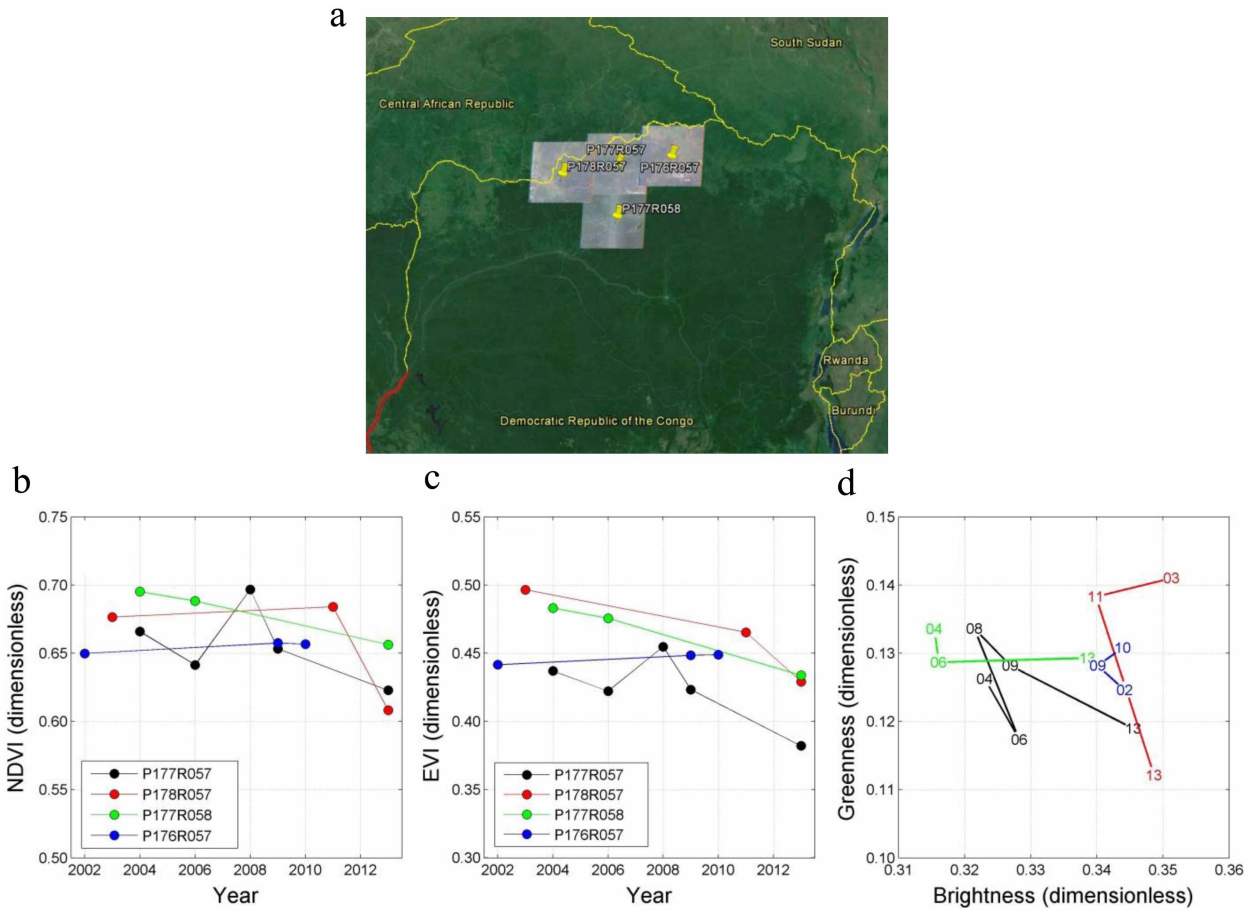
**Extended Data Figure 8 | Simulated surface reflectance values in the MODIS red (RED; a), near-infrared (NIR; b) and blue (BLU; c) bands using the 6S radiative transfer code for 25% overestimation or 25% underestimation of AOT. There are 30 cases (cases 1–10 correspond to a small**

**AOT load, AOT = 0.1; cases 11–20 correspond to a medium AOT load, AOT = 0.3; cases 21–30 correspond to a large AOT load, AOT = 0.5) and the actual reflectance is 0.03, 0.3 and 0.02 in RED, NIR and BLU, respectively (see details in Supplementary Table 1).**



Extended Data Figure 9 | Regional mean anomalies (unitless) and linear trends per decade for MODIS EVI and NDVI. For bidirectional reflectance

distribution function (BRDF)-corrected EVI (a, c) calculated from MCD43C4 and for MODIS NDVI (b, d) from MOD13C2 (as in Extended Data Fig. 4).



**Extended Data Figure 10 | Temporal dynamics of vegetation for four Landsat 7 ETM+ scenes.** **a**, Locations of the Landsat scenes (P176R057, P177R057, P178R057 and P177R058). **b**, Mean temporal variations of NDVI for cloud-free pixels with  $NDVI \geq 0.5$  in the first of the image time series. **c**, Mean temporal variations of EVI for the same pixels as in **b**. **d**, Mean

temporal trajectory of vegetation in the brightness–greenness space of the Tasseled Cap transformation (see details in Supplementary Information section D). A decrease in greenness associated with an increase in brightness signifies forest degradation.